ELECTRONIC SUPPLEMENTARY INFORMATION (ESI)

Formation of Unexpectedly Active Ni-Fe Oxygen Evolution Electrocatalysts by Physically Mixing Ni and Fe Oxyhydroxides

Mikaela Görlin,[*a,b,c] Petko Chernev,[a] Paul Paciok,[d] Cheuk-Wai Tai,[e] Jorge Ferreira de Araújo,[b] Tobias Reier,[b] Marc Heggen,[d] Rafal Dunin-Borkowski,[d] Peter Strasser,[b] and Holger Dau[a]

[a]   Department of Physics, Free University of Berlin, 14195 Berlin, Germany
[b]   The Electrochemical Energy, Catalysis, and Materials Science Laboratory, Department of Chemistry, Technical University of Berlin, 10623 Berlin, Germany
[c]   Department of Physics, AlbaNova University Centre, Stockholm University, SE-10691 Stockholm, Sweden
[d]   Ernst Ruska-Centre for Microscopy and Spectroscopy with Electrons, Forschungszentrum Jülich, Jülich, Germany
[e]   Department of Materials and Environmental Chemistry, Stockholm University, SE-106 91, Sweden

Experimental details

Solvothermal Synthesis of Parental Ni$_{100}$ and Fe$_{100}$ Oxide Catalysts

The parental Ni$_{100}$(OH)$_2$ catalyst was prepared 0.1 M Ni(NO$_3$)$_2$·6H$_2$O (99.999% trace metals basis, Aldrich), and the Fe$_{100}$(OOH) catalyst from 0.1 M Fe(acac)$_3$ (99.95% trace metal basis, Aldrich), to a total amount of 0.44 mmol of metal salt in the reaction solution. The precursor salts were dissolved in benzyl alcohol (Puriss, 99-100.5%), and additions of 0.20 mmol of 1,2-Benzenediol (>99%, Aldrich) to a final reaction volume of 20 ml. As control, co-synthesized Ni-Fe catalysts were prepared by mixing the desired molar ratio of the Ni and Fe metal salts. The reaction mixtures were sealed in special autoclave vials (Anton Paar) and heated to 190 °C for 15 min with a ramping step of 16.5 °C/min. The reactions were quenched by rapid cooling to room temperature. The solid products were collected by washing five times with high purity ethanol using repetitive centrifugation at 7500 rpm for 15 min each washing cycle. To minimize Fe impurities in the Ni$_{100}$ catalyst, the solvents were purified prior to the synthesis according to the method reported by Trotochaud et al.[1]

Preparation of Physically Mixed Ni+Fe Catalysts

After the solvothermal synthesis step, a series of physically mixed (p.m.) Ni+Fe oxide catalysts with various Ni/Fe ratios were obtained by mixing known amounts of the parental Ni$_{100}$(OH)$_2$ and Fe$_{100}$(OOH) catalysts at room temperature. First, two separate ink formulations of the Ni$_{100}$ and Fe$_{100}$ catalysts were prepared by mixing 5 mg of the catalyst powder with 500 µl of Milli-Q, 750 µl of isopropanol, and 10 µl of Nafion (5 wt.%, Sigma). The two Ni$_{100}$ and Fe$_{100}$ catalyst inks were homogenized during 20 min using sonication, still kept as separate inks. The two inks were then mixed to form a series of physically mixed Ni+Fe(OOH) catalysts with different Ni/Fe ratios, by pipetting a known amount (typically 5 µl) of the two inks into new Eppendorf tubes. The inks were mixed for additional ~1 min at room temperature using sonication to form the physically mixed Ni+Fe catalysts. The physically mixed Ni+Fe inks were analyzed with elemental analysis to determine the actual metal content and Ni/Fe ratio and the amount of metal. Thin films were prepared for electrochemical characterization by drop-casting inks corresponding to a catalyst loading of ~100 µg/cm^2 and a total metal loading (Ni+Fe) of ~25 µg/cm^2 onto polished glassy carbon electrodes, and dried in the oven at 60 °C for 8 min. The actual metal loading were determined using elemental analysis.

Elemental Analysis

The metal content of the parental catalyst powders was determined by inductively coupled plasma optical emission spectrometry (ICP-OES), using a Varian 715-ES spectrometer with a CCD detector. The samples were chemically digested in a volume of 2 mL of HNO$_3$:H$_2$SO$_4$:HCl in a ratio of 1:1:3, which were sonicated for 10 min and then left for additional ~2h in the acid. The samples were diluted with Milli-Q water (>18 MΩ cm) to obtain the desired optical emission intensities. The metal content of Ni and Fe of the drop-casted electrodes before and after exposure to OER catalytic potential was determined using total-reflection x-ray fluorescence (TXRF) spectroscopy. The samples were digested by dissolving the catalyst films in a mixture of 250 µl of HCl (37 %, Merck) and 50 µl isopropanol (ACS Reag., VWR) and sonicated for 1 min. Additions of the same amount of a Ga-standard (Merck) with a concentration of 1 mg/mL allowed for quantitative determination of the metal content in the dissolved catalyst films. The TXRF spectra were acquired at 40 kV using a PicoTAX spectrometer (Röntec) with a Si-drift detector.

Electrochemical Characterization

Electrochemical characterization was carried out in a standard three-electrode rotating disk electrode (RDE) setup. Glassy carbon electrodes served as working electrode (Φ = 5 mm), a reversible hydrogen reference electrode (RHE) connected via a Luggin capillary, and a Pt-mesh as counter electrode. The activity of the $Ni_{100}(OH)_2$ catalyst was measured in H_2SO_4 cleaned Nalgene beakers. A Gamry reference 3000/600 potentiostat was used to control the measurements. The uncompensated series resistance (iR-drop) was determined using electrochemical impedance spectroscopy (EIS). Cyclic voltammograms (CVs) were compensated for iR-drop afterwards, and chronoamperometric measurements carried out at iR-compensated potentials. The working electrode was kept at a rotation speed of 1600 rpm during CV scans and at 2200 rpm during the steady-state measurements to avoid blockage due to strong oxygen evolution. The electrolyte concentration was 0.1 M KOH for all measurements (semiconductor grade, 99.99% trace metals basis, Aldrich). The measurements were carried out in electrolyte striped of Fe-impurities (unless otherwise stated) using a purification method reported by Trotochaud et al.[1]

Turnover frequency (TOF) and redox electrons calculations

Turnover frequencies (TOF) were estimated from quasi-stationary state measurements at 1.53 V_{RHE}. The TOF is reported in units of moles of O_2 per second (s^{-1}) based on the total moles of metal (Ni+Fe) that was drop-casted on the electrode (determined by TXRF analysis) according to Eq. S1.

$$TOF = \frac{i_{geom.} \times A}{z \cdot F \cdot n_{Ni+Fe}}$$
(S1)

where $i_{geom.}$ is the current density, A is the working electrode area, z is 4, F is the Faraday constant, and n is the total moles of Ni and Fe on the electrode.

The redox charge (electrons per Ni atoms) was estimated by integrating the area under the anodic and cathodic redox peaks ($Ni^{2+} \rightarrow Ni^{3+/4+}$) from CVs recorded at 10 mV/s, and normalized to the geometric moles of Ni on the electrode obtained by elemental analysis, according to Eq. S2.

$$Redox\ e^- = \frac{Q_{Ni}}{z \cdot F \cdot n_{Ni}}$$
(S2)

where Q_{Ni} is the integrated area under the redox peak (for the $Ni^{2+} \rightarrow Ni^{3+}$ transition), z equals 1 (the number of electrons transferred in the reaction), F is the Faraday constant, and n_{Ni} is the moles of Ni on the electrode.

In situ UV-vis spectroscopy

UV–vis spectra were recorded using a UV/Vis/NIR spectrometer (Avantes, AvaLight-DH-S-BAL) with a deuterium and a halogen lamp. The spectrometer was connected via fiber optics cables to the electrochemical cuvette cell. Spectra were collected between 250-900 nm with a time resolution of ~400 ms. Transparent fluorine-doped tin oxide (FTO) was employed as working electrode (Sigma-Aldrich). The catalysts were drop-casted on an area of ~0.65 cm^2. The electrodes were placed in the path of the beam in a 1 cm quartz cuvette. A leak-free Ag/AgCl reference electrode (Warner Instruments) and a Pt-mesh counter

electrode were placed along the inner walls of the cuvette. All potentials were converted to the RHE scale by $E_{RHE} = 0.21\ V + 0.059V \times pH$ (the real offset was obtained by calibration). The FTO electrodes were cleaned in high purity ethanol by sonication for 5-10 min prior to the measurements, and afterwards rinsed with Milli-Q water. The measurements were performed in 0.1 M KOH. The $Ni_{100}(OH)_2$ catalyst was measured in Fe-free KOH purified according to a reported method.[1]

Differential Electrochemical Mass Spectrometry (DEMS)

Differential Electrochemical Mass Spectrometry (DEMS) was measured in a dual thin layer electrochemical flow-cell in 0.1 M KOH. The volatile products were monitored during the course of a CV scan at 10 mV/s using an electrochemical flow-cell coupled to a Pfeiffer Vacuum QMS 200 mass spectrometer. The inlet was separated by a 150 µm thick microporous PTFE membrane (30 nm pore size, Cobetter). Two pumps (HiPace 80, Pfeiffer) were operating to obtain a differential pressure between the two chambers, with pressures between 10^{-3} to 10^{-6} mbar. Glassy carbon (GC) were used as working electrodes ($\varnothing = 5$ mm, Pine Instruments), as Pt-mesh as counter electrode placed in the outlet of the flow, and a leak-free Ag/AgCl reference electrode placed close to the working electrode. The potentials are reported versus the RHE scale ($ERHE = 0.198V + 0.059V \times pH$). CVs were recorded between ~1-1.57 V_{RHE} (before iR-comp). The Ohmic drop was ~20 Ω. The mass spectrometric ion currents for each mass spectrometric detected volatile product j ($i_{MS,j}$) were converted into the faradaic current contributions, $i_{F,j}^{DEMS}$, using a catalyst-specific sensitivity constant, K_j^*, obtained from steady-state measurements where 100 % O_2 was assumed, according to Eqs. S3-S4.

$$K_j^* = \frac{i_{MS,j} \cdot z}{i_F^{100\%FE}} \tag{S3}$$

$$i_{F,j}^{DEMS} = \frac{i_{MS,j} \cdot z}{K_j^*} \tag{S4}$$

The faradaic efficiency was calculated by excluding the area of the redox peak that is not related to O_2, according to Eq. S5

$$FE\ (\%) = \frac{Q_{F,j}^{DEMS}}{Q_F} \cdot 100 \tag{S5}$$

where $Q_{F,j}^{DEMS}$ and Q_F are the charges the (integrated areas) under the curves.

Electron Microscopy (SEM,TEM) and EDX Elemental Mapping

SEM characterization was carried out at ZELMI Zentrum Berlin. The catalysts were drop-casted on glassy carbon electrodes with a geometric area of 2 cm^2. Scanning electron micrographs (SEM) were acquired on a Hitachi field emission SEM microscope (FE-SEM) type SU8030 with a cold field emitter. The SEM images were taken with an accelerating voltage of 8 kV. Energy dispersive x-ray (EDX) metal mapping analysis were acquired using a ZEISS DSM982 SEM microscope equipped with an EDAX TEAM system with a 10 mm^2 silicon drift detector (Apollo XP). The measurements were carried out at 15 keV primary beam energy. Quantifications of the Ni and Fe were obtained from the K-lines.

The samples were dispersed on the copper TEM supporting grid with holey carbon films for transmission electron microscopy analysis. The analysis of the particles by HAADF-STEM analysis was conducted using a

FEI Titan 80-200 (ChemiSTEM) electron microscope at Ernst-Ruska Center for Microscopy and Spectroscopy with Electrons, Jülich. The microscope was operated at 80 kV, and equipped with a spherical aberration (Cs) probe corrector (CEOS GmbH) and a high-angle annular dark field (HAADF) detector. A probe semi-angle of 17.7 mrad and a detector inner collection semi angle of 88 mrad were used. Compositional maps were obtained with energy-dispersive X-ray spectroscopy (EDX) using four large-solid-angle symmetrical Si drift detectors. For EDX analysis, Ni K and Fe K peaks were used.

Further analysis with Electron energy loss spectroscopy (EELS), STEM, and energy-filtered TEM (EFTEM) were carried out in a JEOL JEM-2100F field-emission microscope at the Department of Materials and Environmental Chemistry at Stockholm University. The microscope was operated at 200 kV (Cs = 0.5 mm, Cc = 1.1 mm, point resolution = 1.9 Å, lattice resolution = 1.0 Å) equipped with a Gatan Ultrascan 1000 camera, a Gatan annular dark-field (ADF) detector and a post-column Gatan Imaging Filter (Trdiem 863). HAADF-STEM images were acquired with a probe size of 0.5 nm and in HAADF5 mode. EELS spectra of the selected regions of interest were processed in Gatan GMS suits, that did background subtraction and removed the plural scattering. EFTEM images were obtained by extract the core-loss information of the elements by applying three-window method. The positions of each element edge (O K-edge and the $L_{3,2}$ edge of Fe and Ni) were determined in advance. The results of EFTEM and thickness variation of the selected regions are presented in pseudo-color.

X-ray Absorption Spectroscopy (XAS)

X-ray absorption spectroscopy was measured at the Ni and Fe K-edges at the BESSY-II synchrotron facility at the KMC-1 and KMC-3 beamlines (Helmholtz-Zentrum Berlin, Germany) for quasi-*in situ* and *operando* measurements, respectively. The quasi-*in situ* measurements were carried out at cryogenic temperatures (20 K) using a liquid-helium cryostat[2] and a 13-element energy-resolving Ge detector (Canberra) to detect the X-ray fluorescence. The catalysts were freeze-quenched in liquid nitrogen after kept at an electrode potential of 1.63 V_{RHE} for 30 min in 0.1 M KOH.[3, 4] The samples were stored in liquid nitrogen until analyzed at the BESSY-II synchrotron facility. The *operando* XAS studies were carried out at room temperature in a standard three-electrode electrochemical PTFE cell, at the KMC-3 beamline (BESSY-II, HZB). The catalysts were drop-casted on thin glassy carbon electrodes (~100 μm thickness, HTW GmbH), and positioned at an angle of 45° towards the incoming beam. The fluorescence was detected using backside illumination with an x-ray scintillation detector and a photomultiplier positioned at an angle of 45° with respect to the sample. The scintillation detector was covered with a thin foil of Al, and an additional metal foil one element below the investigated K-edge to reduce the scattered light.

The k^3-weighted extended X-ray absorption fine structure (EXAFS) spectra were extracted using the E_0 value of 8334 eV for Ni and 7117 eV for Fe. The simulations of the EXAFS spectra were carried out using in-house software (SimX Lite). Phase functions were generated from atomic structures of layered $Ni(OH)_2$ and $Fe(OOH)$ using the FEFF software package version 9.1 with self-consistent field.[5, 6] The amplitude reduction factor (S_0^2) was set to 0.85 for both Ni and Fe K-edges. The simulations were carried out between 25-801 eV above E_0 for the Ni K-edge (k-range of 2.6 -14.5 Å^{-1}) and between 25-595 eV for Fe K-edge (k-range 2.6 - 12.5 Å^{-1}). The simulations were fitted to experimental data and optimized in k-space by the least-squares method using Levenberg-Marquardt algorithm with numerical derivatives. The error ranges of the fit parameters were estimated from the covariance matrix at a 68 % confidence interval. [7]
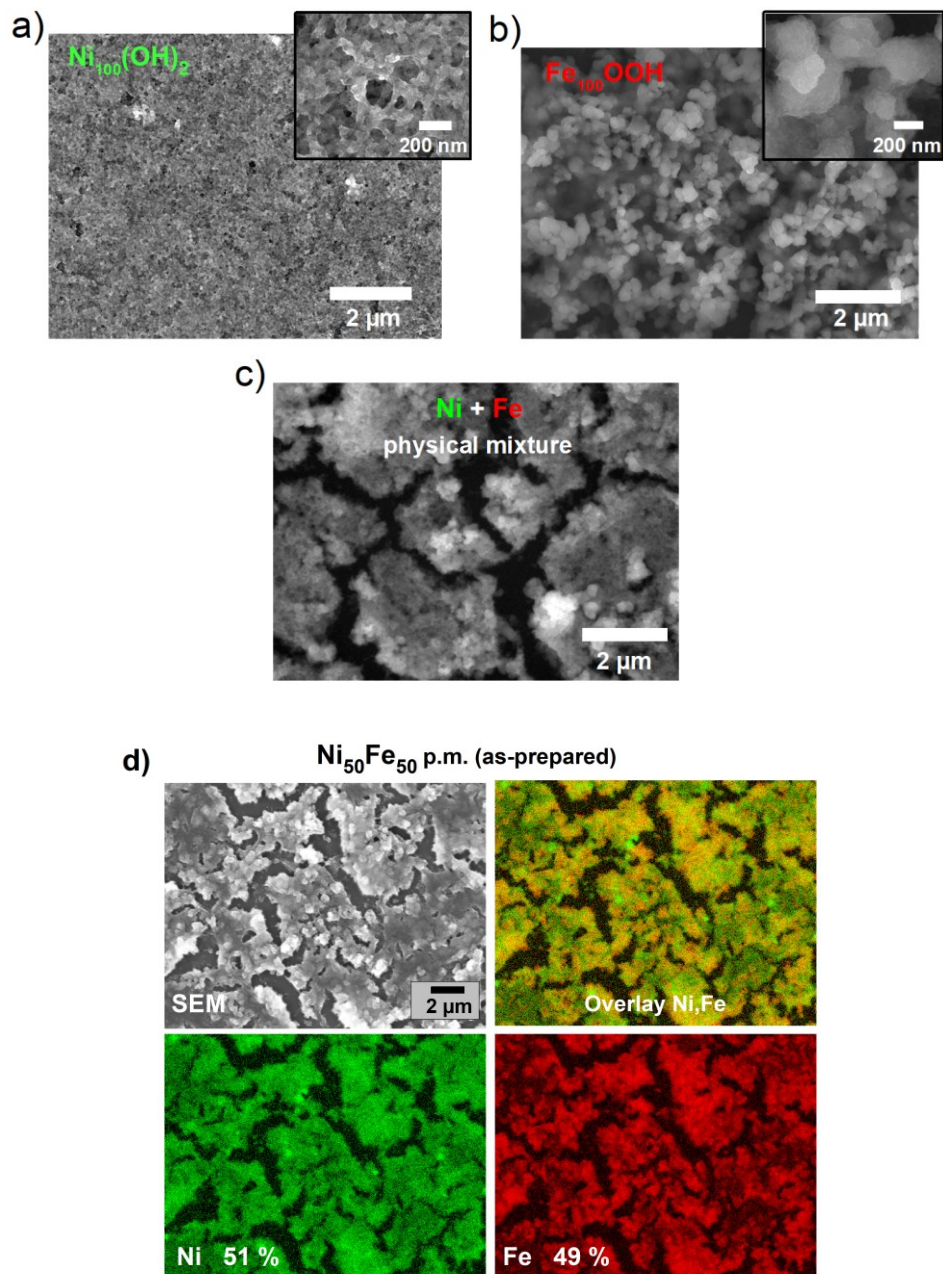
Scanning Electron Microscopy (SEM)

Fig. S1. Scanning electron micrographs (SEM) images of **(a)** the parental $Ni_{100}(OH)_2$ **(b)** the parental $Fe_{100}(OOH)$ **(c)** the physically mixed (p.m.) $Ni_{50}+Fe_{50}$ catalyst. **(d)** SEM images a $Ni_{50}+Fe_{50}$ p.m. catalyst in the as-prepared state (top left) and the corresponding EDX elemental mappings of Ni and Fe (bottom). The EDX Ni and Fe overlay is shown to the upper right. The compositions are given in at. %, estimated from the metal K-lines of the displayed areas.
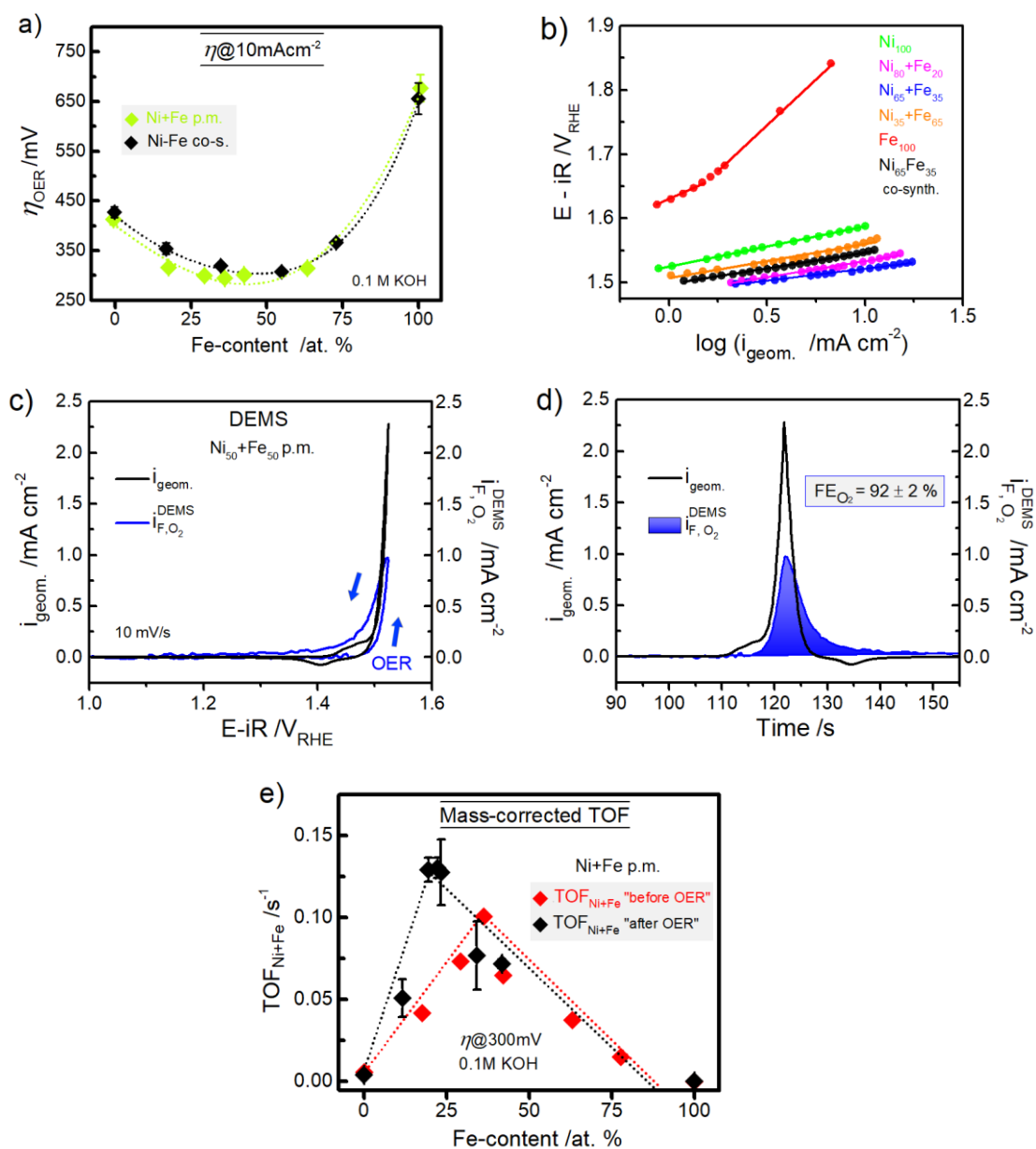
OER activity characterization

Fig. S2. (a) Overpotential (η) at 10 mA cm^{-2}. **(b)** Tafel plots of Ni+Fe p.m. catalysts with different stochiometries of Ni(OH)$_2$:Fe(OOH), estimated from CVs at 5 mV/s in 0.1 M KOH using the cathodic sweep where the faradaic current can be separated from the redox contributions. **(c)** Differential electrochemical mass spectrometry (DEMS) of a p.m. Ni$_{50}$+Fe$_{50}$ catalyst, the O$_2$ evolved during a CV at 10 mV/s. The blue arrows mark the direction of the scan. **(d)** The data in (d) shown in the time domain. The black curves represent the current densities from the potentiostat (i$_{geom.}$) and the blue curves the faradaic mass spectrometric ion currents for m/z = 32 (i$\frac{MS}{F,O2}$) (see Eqs. S3-S5). The measurements were carried out in 0.1 M KOH, at a metal loading of ~10 μg $_{Ni+Fe}$cm^{-2}. **(e)** TOF$_{Ni+Fe}$ based on the moles of Ni+Fe on the electrode before OER characterization ("before OER") and at the end of the OER characterization after ~2 h ("after OER"). The values were estimated using TXRF analysis.

Table S1. Extracted activity parameters for our physically mixed Ni-Fe catalysts in 0.1 M KOH.

Catalyst	Electrolyte	Catalyst loading $(\mu g/cm^2)$	Metal loading $(\mu g_{Ni+Fe}/cm^2)$	$i@\eta_{OER}=$ 300 mV (mA/cm^2)	η_{OER} @ I = 10 mAcm^{-2} (mV)	TOF$_{Ni+Fe}$ (s^{-1})	Tafel slope (mV/dec)
Ni$_{100}$(OH)$_2$	0.1 M KOH*	100	21	0.4	402	0.003	58
Ni$_{80}$+Fe$_{20}$	0.1 M KOH*	100	25	6.5	311	0.040	56
Ni$_{65}$+Fe$_{35}$	0.1 M KOH*	100	20	13.0	298	0.098	37
Ni$_{35}$+Fe$_{65}$	0.1 M KOH*	100	24	6.8	325	0.045	49
Ni$_{20}$+Fe$_{80}$	0.1 M KOH*	100	20	2.5	342	0.016	53
Fe$_{100}$(OOH)	0.1 M KOH	100	17	0.01	663	0.0001	65
							280 (± 100)

* The electrolyte was stripped of Fe-impurities according to a reported purification method [1]
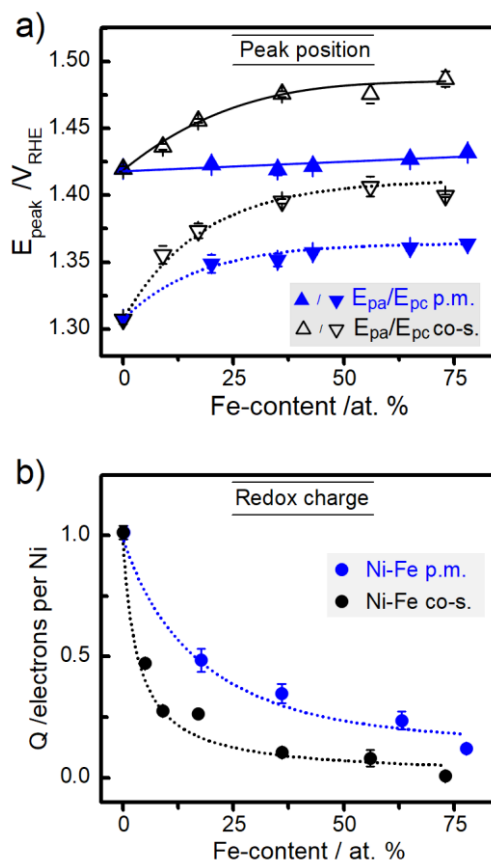
The Ni(OH)₂→Ni(OOH) redox transition

Fig. S3. (a) Peak positions of the $Ni^{2+} \rightarrow Ni^{3+/4+}$ redox transition, anodic, E_{pa} (*tip-up triangles*), cathodic E_{pc} (*tip-down triangles*), extracted from CVs at 10 mV/s. **(b)** integrated peak area (redox charge) for the $Ni^{2+} \rightarrow Ni^{3+/4+}$ transition, shown as electrons transferred per Ni atoms. The physically mixed (p.m.) Ni+Fe catalysts (*blue symbols*) and the co-synthesized (co-s.) Ni-Fe catalysts (*black symbols*). The data was obtained from CVs at 10 mV/s after application of 1.63 V for 30 min in 0.1 M KOH. The redox charge calculations are shown in Eq. S2.
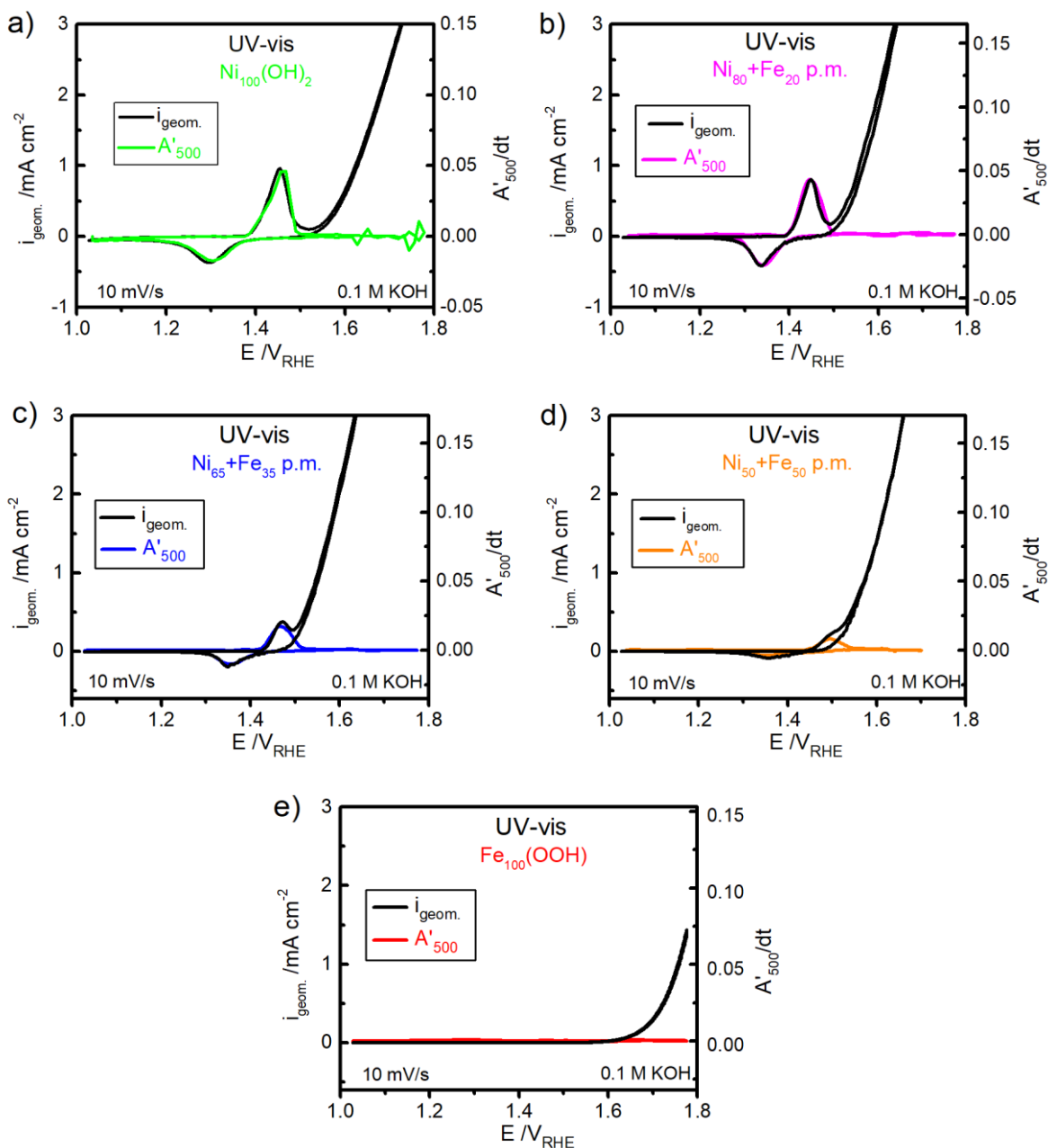
In situ UV-vis spectroelectrochemistry

Fig. S4. In situ UV-vis spectroelectrochemistry shown as the first derivative (A'/dt) of the absorption at $\lambda=500$ nm during a CV cycle at 10 mV/s in 0.1 M KOH. **(a)** parental $Ni_{100}(OH)_2$ **(b)** $Ni_{80}+Fe_{20}$ p.m. **(c)** $Ni_{65}+Fe_{35}$ p.m. **(d)** $Ni_{50}+Fe_{50}$ p.m. **(e)** parental $Fe_{100}(OOH)$. The UV-vis traces are shown as *colored curves* and the current density as *black curves*. Conductive FTO electrodes were employed as working electrode (0.65 cm^2), a Pt-mesh as counter electrode, and a leak-free Ag/AgCl as reference electrode (see Fig. S5a below for demonstration of the UV-vis setup). The CVs are shown without iR-correction, and the uncompensated solution resistance in the UV-vis setup was estimated to 20 Ohm.
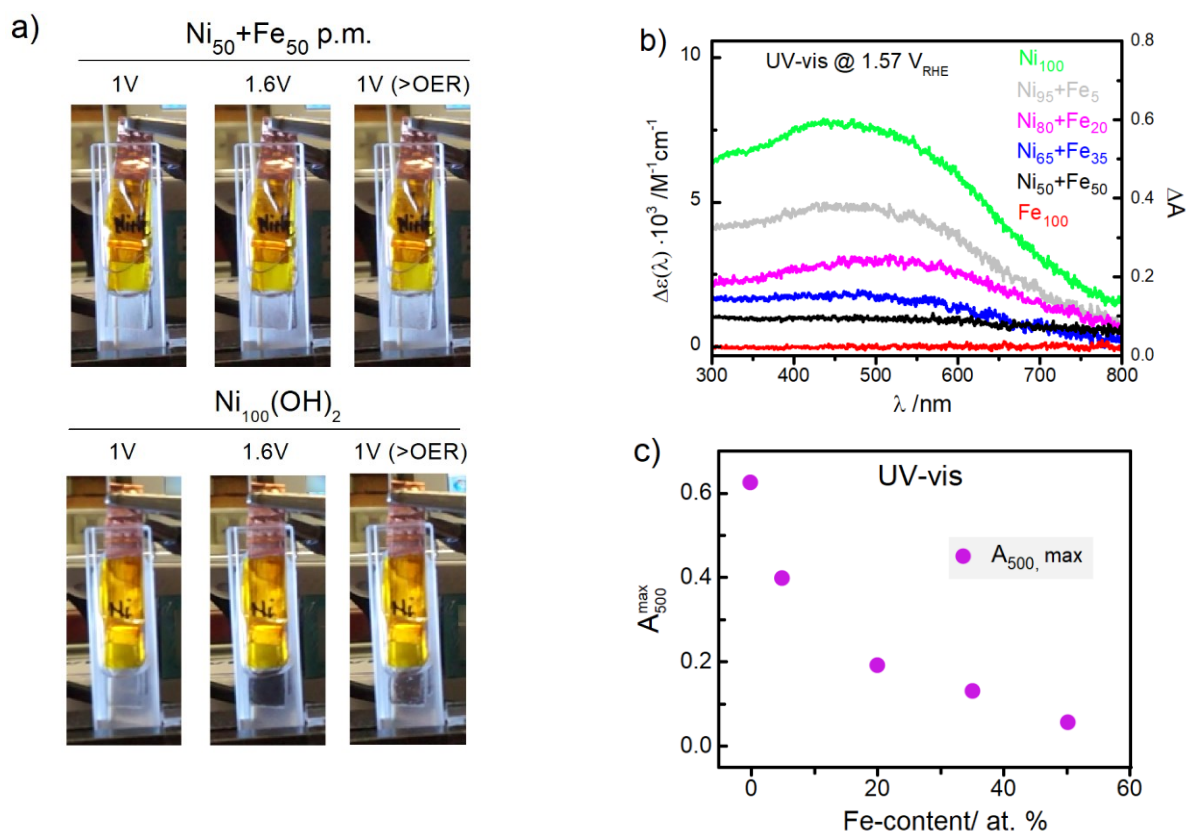
Fig. S5. In situ UV-vis measurements on conductive FTO electrodes **(a)** $Ni_{50}+Fe_{50}$ p.m. catalyst (*top*) and the parental $Ni_{100}(OH)_2$ catalyst (*bottom*) at 1V, 1.6 V and back to 1 V after OER (1V >OER). Capton tape was used to define the electrode area and to shield off the Cu-strip (used to connect the working electrode) from the electrolyte. **(b)** UV-vis absorption spectra at 1.57 V. **(c)** The maximum of the UV-vis absorption at λ=500 nm, obtained from the measurements in (b). All measurements were carried out in 0.1 M KOH at a metal loading of ~5 µg/cm^2 with respect to the Ni-content.
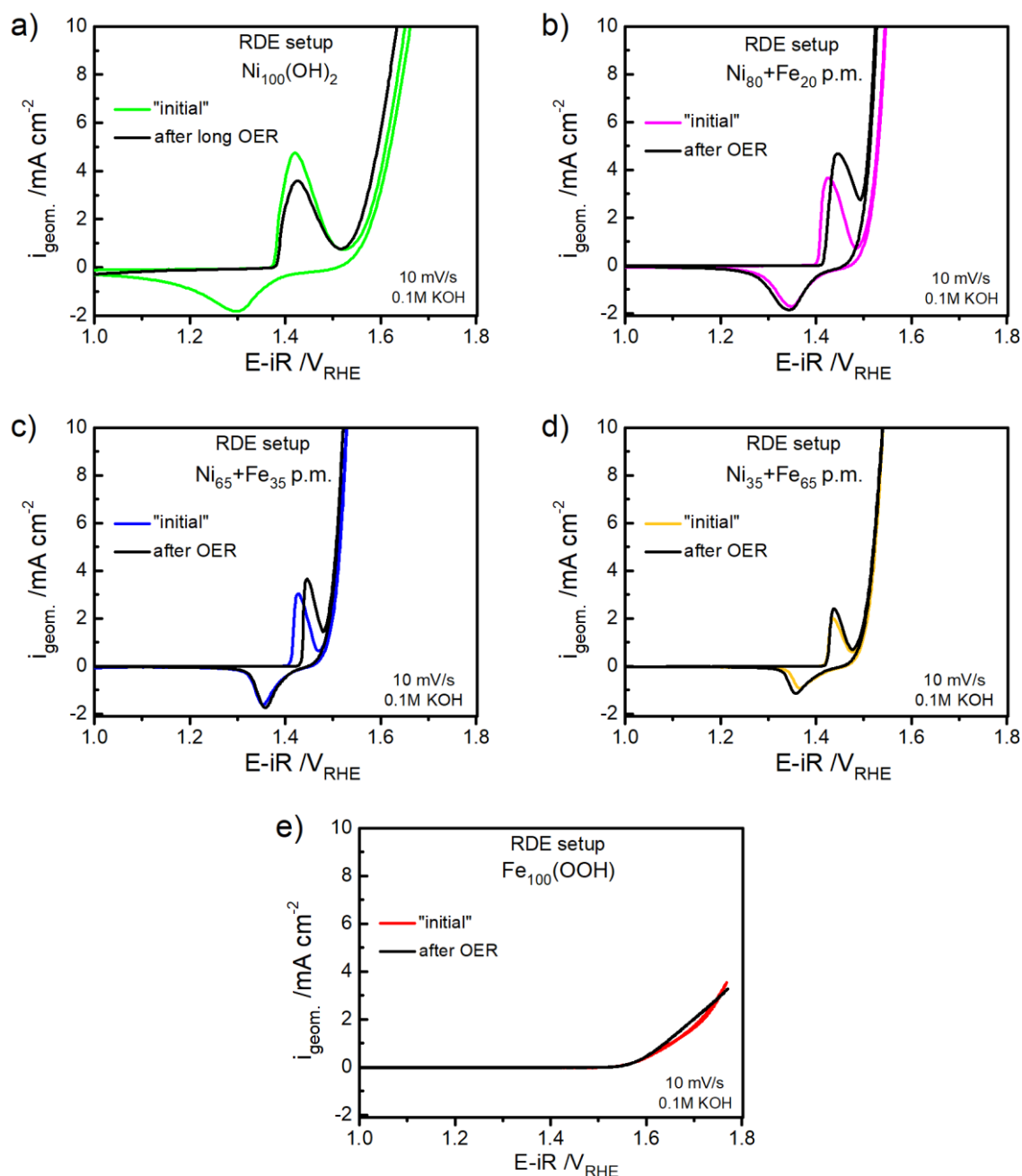
"Activation" during OER characterization

Fig. S6. CVs of physical mixtures (p.m.) right after 1.63 V for 30 min used for activation and at the end of the entire OER characterization protocol of ~2 h. **(a)** $Ni_{100}(OH)_2$ **(b)** $Ni_{80}+Fe_{20}$ p.m. **(c)** $Ni_{65}+Fe_{35}$ p.m. **(d)** $Ni_{35}+Fe_{65}$ p.m. **(e)** $Fe_{100}(OOH)$. All measurements were carried out in RDE setup in Fe-free 0.1 M KOH [1] at a metal loading of 18 ± 4 µg/cm^2 of Ni, at a scan-rate of 1600 rpm.
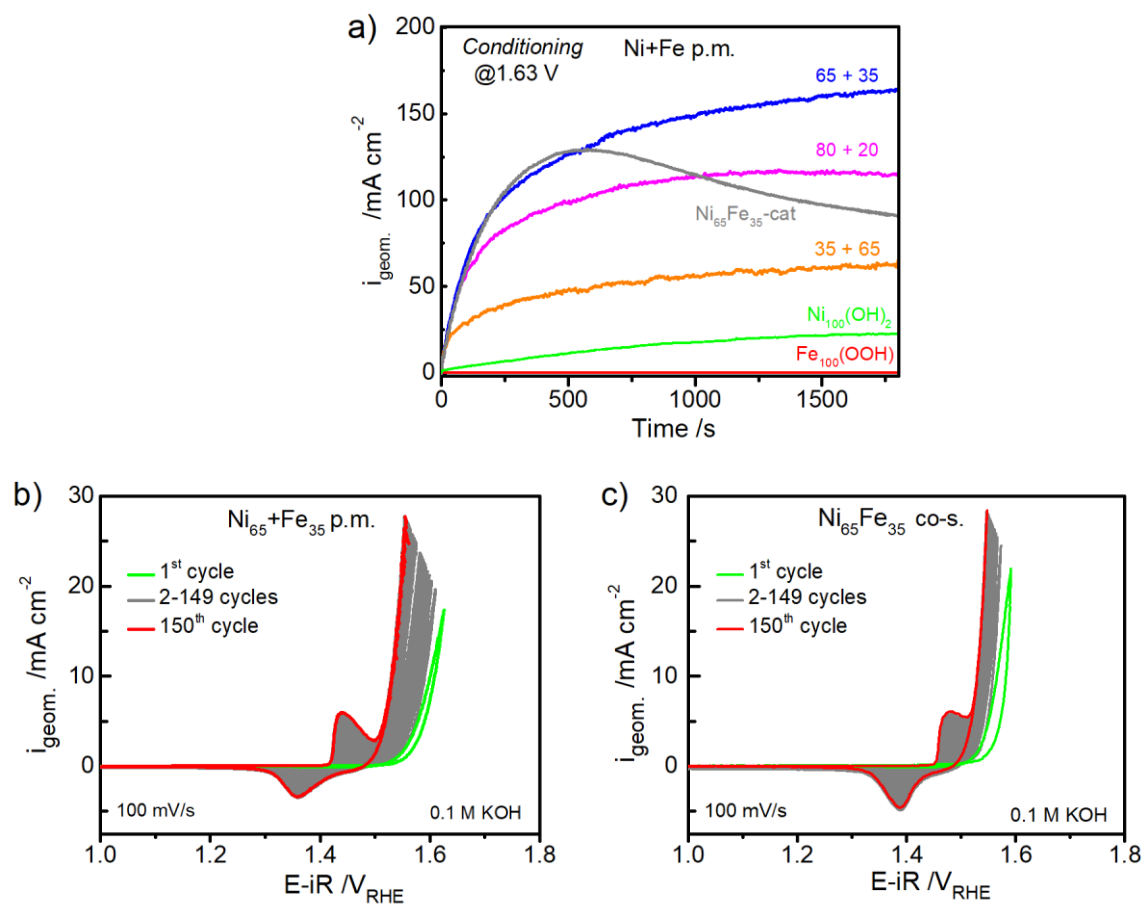
Fig. S7. (a) Application of 1.63 V for 30 min of p.m. Ni+Fe catalysts. **(a)** CV cycle 1-150 of the $Ni_{65}+Fe_{35}$ p.m. catalyst. **(b)** CV cycle 1-150 of the co-s. $Ni_{65}Fe_{35}$ catalyst. Shown are the 1st CV cycle *(green)*, cycle 2-149 *(gray)*, and cycle 150 *(red)*. The measurements were carried out in RDE setup at 1600 rpm at 100 mV/s, and the loading kept at 18 ± 4 µg cm^{-2} total metal (Ni+Fe).

HAADF-STEM and EDX elemental mapping

$Ni_{50}+Fe_{50}$ p.m. as-prepared

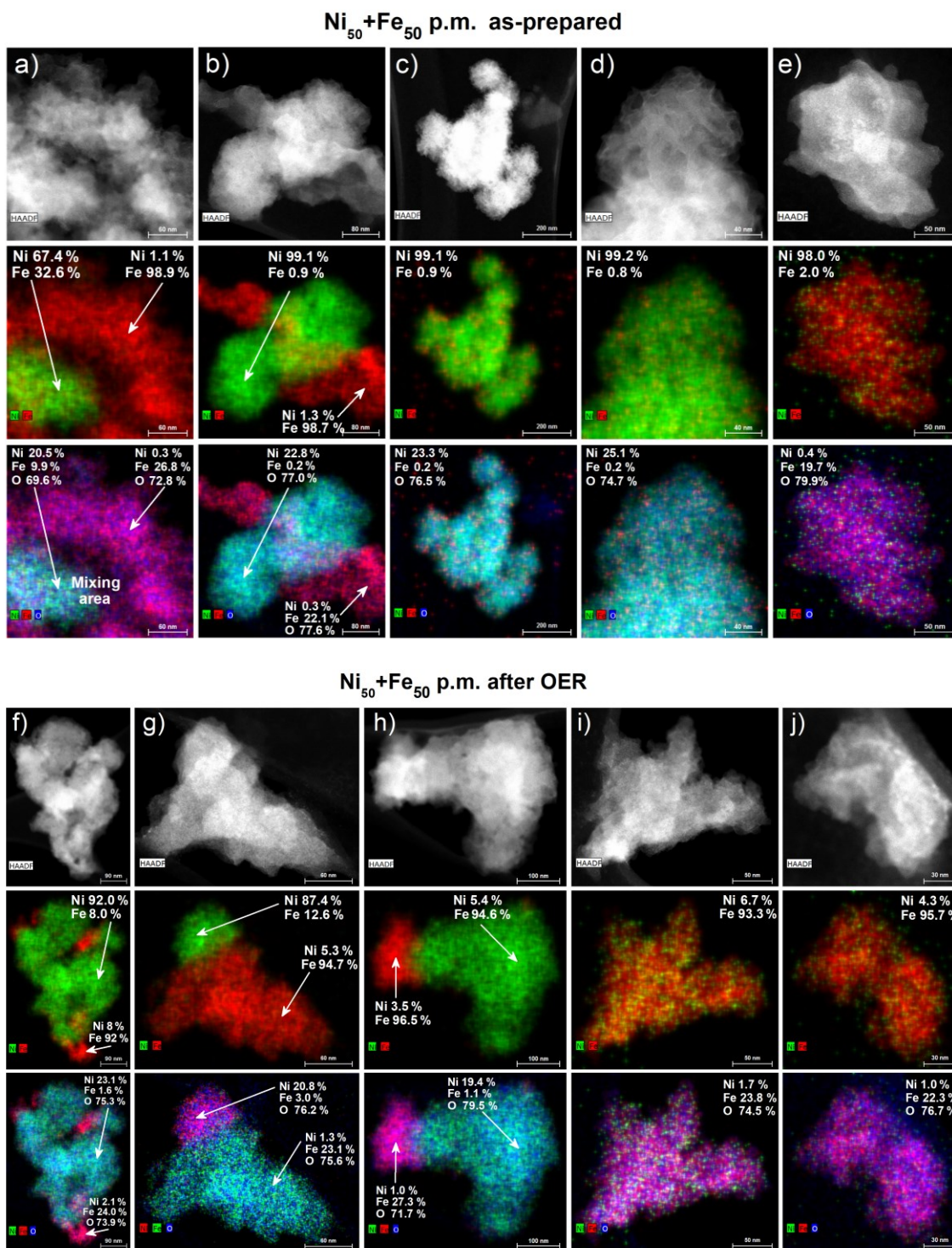## $Ni_{50}+Fe_{50}$ p.m. after OER

Fig. S8. HAADF-STEM images (*upper*), the corresponding EDX elemental mapping overlays of Ni and Fe (*middle*), and overlays of Ni, Fe and O (*lower*), of a $Ni_{50}+Fe_{50}$ physically mixed (p.m.) catalyst. **(a-e)** as-prepared $Ni_{50}+Fe_{50}$ p.m. catalyst **(f-j)** $Ni_{50}+Fe_{50}$ p.m. catalyst after OER, conditioned at 1.63 V for 30 min in 0.1 M KOH.

Ni$_{100}$(OH)$_2$ as-prepared
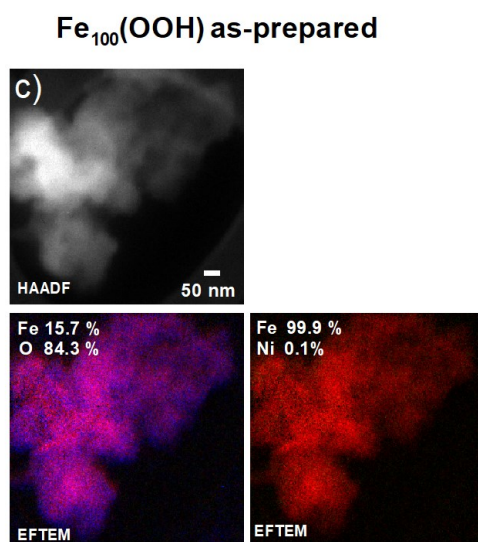
Fe$_{100}$(OOH) as-prepared
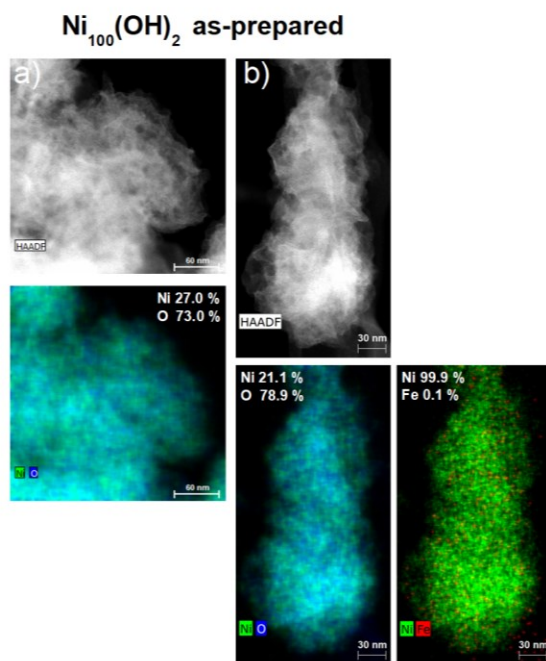
Fig. S9. (a)-(b) HAADF-STEM images (*upper*) and the corresponding EDX elemental mappings and overlays of Ni, Fe, O (lower) of the parental as-prepared Ni$_{100}$(OH)$_2$ catalyst. **(c)** HAADF-STEM (*upper*) and elemental energy filtered transmission electron microscopy (EFTEM) mappings with overlays of Ni, Fe,O (*lower*) of the as-prepared parental Fe$_{100}$(OOH) catalyst.

Physical mixture compared the co-synthesized Ni-Fe catalyst

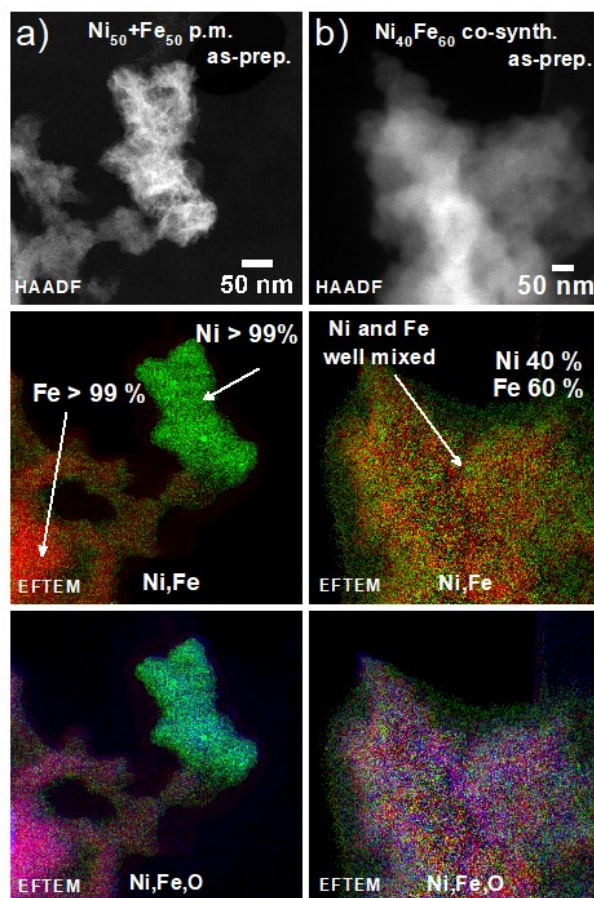**Fig. S10.** HAADF-STEM and elemental energy filtered transmission electron microscopy (EFTEM) mappings of **(a)** as-prepared $Ni_{50}+Fe_{50}$ physical mixture **(b)** as-prepared co-synthesized $Ni_{40}Fe_{60}$ catalyst. Shown are the HAADF-STEM images of the selected regions (*top*) and the corresponding EFTEM elemental map overlays of Ni, Fe (*middle*) and Ni, Fe, O (*bottom*).
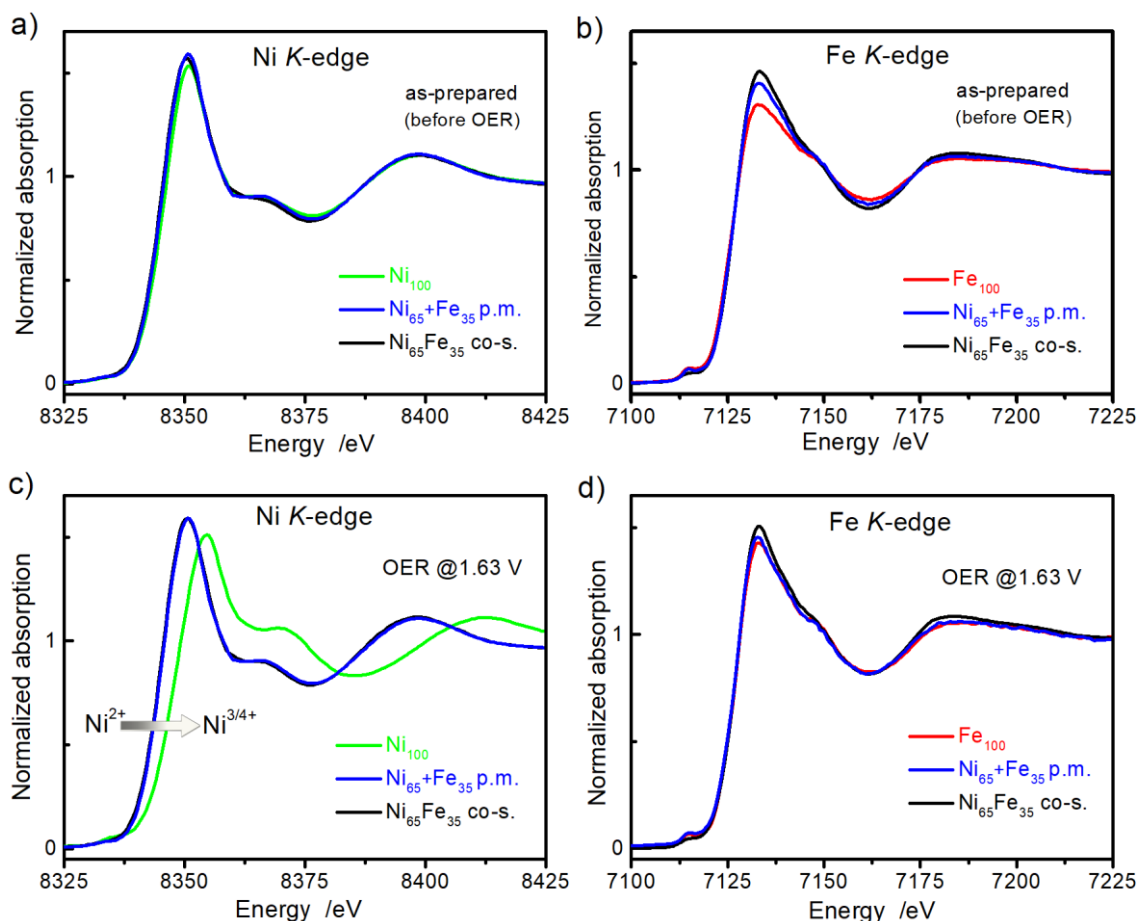
X-ray Absorption Spectroscopy (XAS)

Fig. S11. X-ray absorption near edge spectroscopy (XANES) in the quasi-in situ setup, of samples freeze-quenched at the given potential and measured at 20 K. **(a)** Ni K-edge of as-prepared catalysts (before OER). **(b)** Fe K-edge of as-prepared catalysts (before OER). **(c)** Ni K-edge of catalysts at freeze-quenched at OER catalytic potential of 1.63 V_{RHE} **(d)** Fe K-edge of catalysts at 1.63 V_{RHE}. Shown are the $Ni_{100}(OH)_2$ (*green*), physically mixed (p.m.) $Ni_{65}+Fe_{35}$ (*blue*), co-synthesized (co-s.) $Ni_{65}Fe_{35}$ (*gray*), and $Fe_{100}(OOH)$ (*black*). The catalysts at OER were conditioned at 1.63 V_{RHE} for 30 min in 0.1 M KOH prior to freeze quenching in liquid N_2 at the given potential.
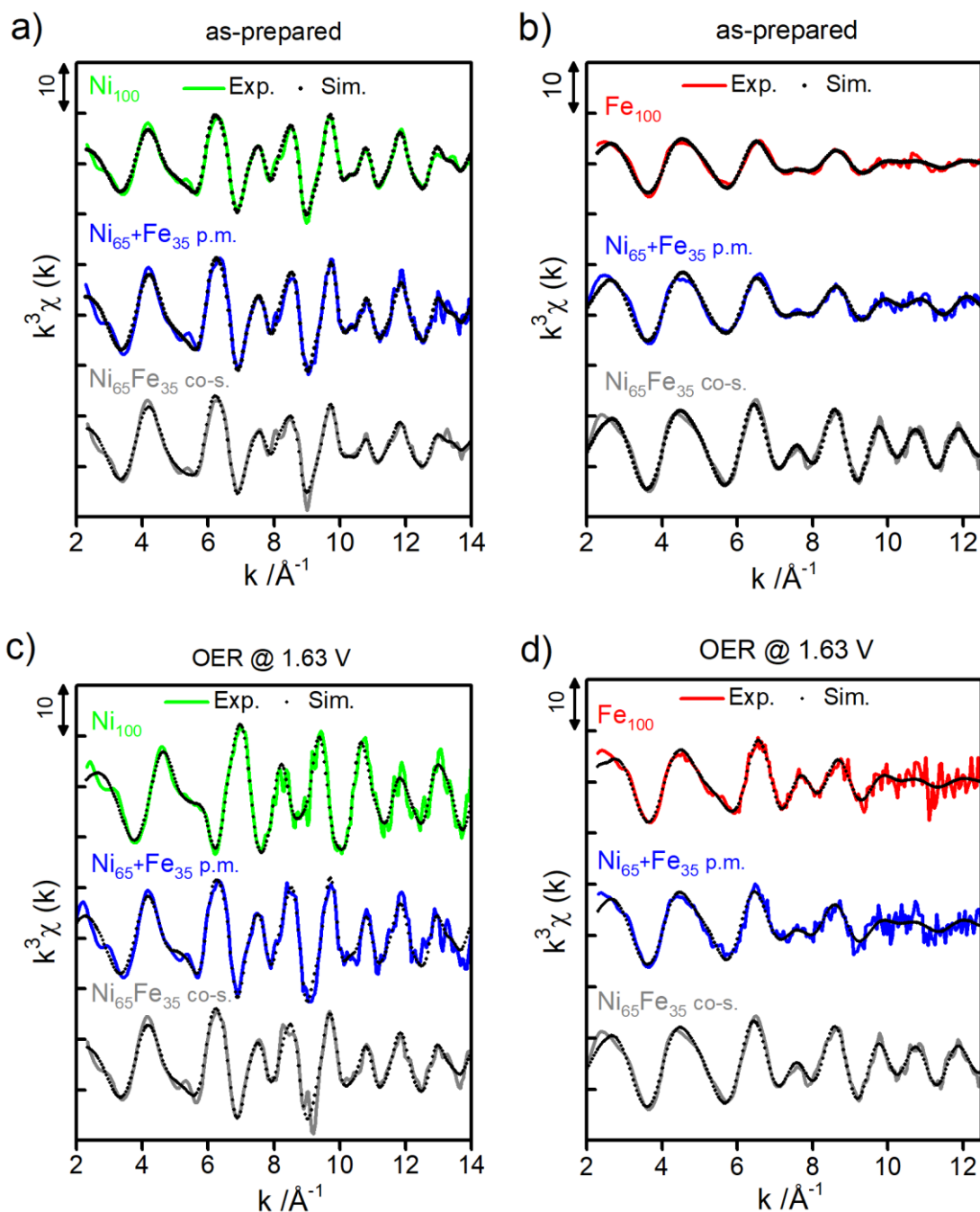
Fig. S12. Extended X-ray absorption fine structure (EXAFS) in the quasi in-situ setup measured at 20 K. (**a**) Ni K-edge of the as-prepared catalysts (before OER). (**b**) Fe K-edge of the as-prepared catalysts (before OER). (**c**) Ni K-edge of catalysts at 1.63 V_{RHE}. (**d**) Fe K-edge of catalysts at 1.63 V_{RHE}. Shown are $Ni_{100}(OH)_2$ (*green*), co-s. $Ni_{65}Fe_{35}$ catalyst (*gray*), p.m. $Ni_{65}+Fe_{35}$ catalyst (*blue*), and $Fe_{100}(OOH)$ (*black*). The catalysts at OER were conditioned at 1.63 V_{RHE} for 30 min in 0.1 M KOH prior to freeze quenching at the given potential in liquid nitrogen. The catalyst compositions are given in at. %.

Operando X-ray absorption spectroscopy
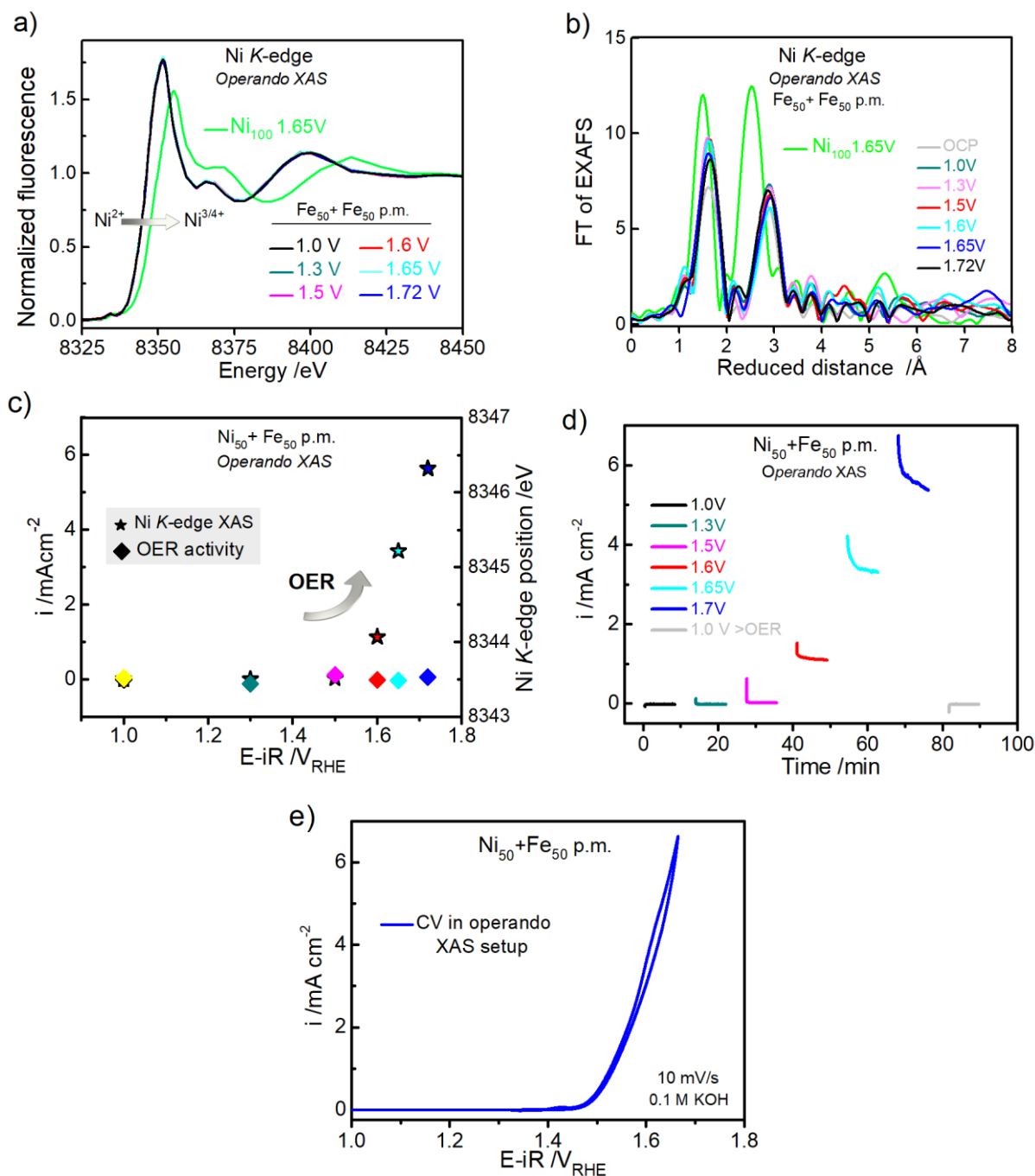
Fig. S13. Operando XAS of the Ni$_{50}$+Fe$_{50}$ p.m. catalyst. **(a)** Ni K-edges of the Ni$_{50}$+Fe$_{50}$ p.m. at different electrode potentials, and of the parental Ni$_{100}$(OH)$_2$ catalyst. **(b)** The corresponding k^3-weighted FT-EXAFS. **(c)** The average activity during steady state conditions (*right axis*) and the Ni K-edge positions (*left axis*). **(d)** The activity during steady state during the collection of XAS spectra. **(e)** CV in the operando XAS setup at 10 mV/s. All measurements were carried out in 0.1 M KOH.

Table S2. Literature comparison of activities of different Ni-Fe oxides measured in 0.1 M KOH electrolyte.

Catalyst	Support	Synthesis method	Electrolyte	Working electrode	Catalyst loading ($\mu g/cm^2$)	Metal loading ($\mu g/cm^2$)	TOF @ $\eta=300mV$ (s^{-1})	ηOER@ 10mA cm^{-2} (mV)	Tafel slope (mV/dec)	Reference
$Ni_{65}+Fe_{35}(O_xH_y)$	Physical mixture	Solvothermal+ sonication	0.1 M KOH (*Fe-free)	GC	100	25	0.10	295	37	*This work
Ni-foam +Fe(NO$_3$)$_3$	Ni-foam	in situ formation	0.1 M KOH	Ni-foam 2×4 cm 380 gm^{-2}	-	-	-	270 (1 min) 230(1h)	43	Yin (2018) [8]
$Ni_{70}Fe_{30}$	Ketjen Black	Sonochemical	0.1 M KOH	GC	140	-	0.025	292	30.4	Lee (2018) [9]
$Ni_{50}Fe_{50}$		Sonochemical	0.1 M KOH	GC	800		-	290	31	Li (2017) [10]
Ni_3Fe_1-LDH	N-doped graphene	Hydrothermal	0.1 M KOH	GC	250	-	-	337	45	Tang (2015) [11]
$Ni_{60}Fe_{40}O_x$	-	Photochemical	0.1 M KOH	FTO	-	-	-	250 (@1 mA/cm^2)	34	Smith (2013) [12]
Porous NiFeO$_x$	-	Co-precipitation	0.1 M KOH	GC	139	-	0.12 (η=387 mV)	328	42	Qi (2015) [13]
$Ni_{45}Fe_{55}(O_xH_y)$	-	Solvothermal	0.1 M KOH	GC	25	5	0.18	330	30	Görlin (2017) [15]
$Ni_{45}Fe_{55}(O_xH_y)$	-	Solvothermal	0.1 M KOH	GC	50	10	0.14	310	35	Görlin (2016) [16]
$Ni_{62}Fe_{38}(O_xH_y)$/C	Vulcan	Solvothermal	0.1 M KOH	GC	200	8	0.45	288	29	Görlin (2015) [14]
$Ni_{80}Fe_{20}$-LDH	-	Hydrothermal	0.1 M KOH	GC	200	-	-	297	-	Dresp (2018) [22]
$Fe_{78}Fe_{22}$ -LDH	Vulcan	Hydrothermal	0.1 M KOH	GC	200	-	-	320	-	Dresp (2016) [23]
$Ni_{78}Fe_{22}$/ Fe-N-C – LDH (1:1)	Vulcan/ PANI	Hydrothermal	0.1 M KOH	GC	200	-	-	285	-	Dresp (2016) [23]
$Ni_{87}Fe_{13}$-LDH	Vulcan XC-72R	Hydrothermal	0.1 M KOH	GC	100	7.9	0.03	360	51	Dionigi (2016) [18]
Ni_3Fe_1-LDH	oGSH	Hydrothermal	0.1 M KOH	GC	250	-	-	350	54	Zhu (2015) [17]
Ni_3Fe_1-LDH	-	Hydrothermal	0.1 M KOH	GC	100	-	-	270	33.6	Xu (2015) [21]
Ni_3Fe_1-LDH	Ni-foam	Hydrothermal	0.1 M KOH	Ni-foam	1000	-	-	250 [a]	50	Lu (2014) [19]
Ni_5Fe_1-LDH	CNT	Hydrothermal	0.1 M KOH	CFP	250	-	-	308	35	Gong (2013) [20]
Ni_3Fe_1/NF	Ni-foam	Electro-deposition	0.1 M KOH	Ni-foam	32	-	0.075 (η=400mV)	240	33	Lu (2015) [25]
$Ni_{60}Fe_{40}(O_xH_y)$	-	Electro-deposition	0.1 M KOH	Au	27 [a]		0.3 [a]	280	40	Louie (2013) [24]

[a] = calculated/estimated by us from the reported data (some of the values were also reported by us in a previous review paper.[26])

Table S3. Fit parameters for the Ni and Fe *K*-edge of the $Ni_{100}(OH)_2$ and $Fe_{100}(OOH)$, the physical mixture (p.m.) $Ni_{65}+Fe_{35}$, and the co-synthesized (co-s.) Ni-Fe catalyst. The parameters were obtained from XAS measurements in the quasi-in situ setup at 20 K.

as-synthesized (before OER)								
Catalyst	*K*-edge	R(M-O) /Å	CN	σ /Å	R(Ni-M) /Å	CN	σ /Å	R_f
$Ni_{100}(OH)_2$	Ni	2.04 ± 0.01	5.2 ± 0.4	0.07 ± 0.01	3.08 ± 0.01	5.4 ± 0.7	0.07 ± 0.01	16.8
$Ni_{65}+Fe_{35}$ p.m.	Ni	2.04 ± 0.01	6.3 ± 0.4	0.07 ± 0.01	3.08 ± 0.01	5.7 ± 0.6	0.07 ± 0.01	17.1
$Ni_{65}Fe_{35}$ co-s.	Ni	2.04 ± 0.01	6.2 ± 0.5	0.07 ± 0.01	3.08 ± 0.01	5.2 ± 0.8	0.08 ± 0.01	18.0
$Fe_{100}(OOH)$	Fe	1.98 ± 0.01	3.0 ± 0.3	0.06 ± 0.01	3.08 ± 0.03	0.8 ± 0.4	0.07 ± 0.01	26.3
$Ni_{65}+Fe_{35}$ p.m.	Fe	1.98 ± 0.01	4.2 ± 0.3	0.06 ± 0.01	3.06 ± 0.02	1.7 ± 0.4	0.07 ± 0.01	29.5
$Ni_{65}Fe_{35}$ co-s.	Fe	2.00 ± 0.01	4.7 ± 0.3	0.06 ± 0.01	3.10 ± 0.01	1.9 ± 0.4	0.07 ± 0.01	27.0
@ catalytic OER potential (1.63 V_{RHE}) in 0.1 M KOH								
	K-edge	R(M-O) /Å	CN	σ /Å	R(Ni-M) /Å	CN	σ /Å	R_f
$Ni_{100}(OH)_2$	Ni	1.87 ± 0.01	5.2 ± 0.4	0.07 ± 0.01	2.82 ± 0.01	5.9 ± 0.4	0.07 ± 0.01	21.9
$Ni_{65}+Fe_{35}$ p.m.	Ni	2.04 ± 0.01	6.3 ± 0.5	0.07 ± 0.01	3.08 ± 0.01	6.5 ± 0.6	0.07 ± 0.01	20.3
$Ni_{65}Fe_{35}$ co-s.	Ni	2.04 ± 0.01	6.4 ± 0.5	0.07 ± 0.01	3.08 ± 0.01	6.3 ± 0.7	0.07 ± 0.01	21.0
$Fe_{100}(OOH)$	Fe	1.99 ± 0.01	3.8 ± 0.4	0.06 ± 0.01	3.04 ± 0.02	1.6 ± 0.4	0.07 ± 0.01	26.0
$Ni_{65}+Fe_{35}$ p.m.	Fe	2.00 ± 0.01	4.0 ± 0.3	0.06 ± 0.01	3.10 ± 0.02	1.3 ± 0.4	0.07 ± 0.01	27.1
$Ni_{65}Fe_{35}$ co-s.	Fe	2.01 ± 0.01	4.8 ± 0.3	0.06 ± 0.01	3.11 ± 0.01	4.1 ± 0.4	0.07 ± 0.01	23.9

Simulations at the Fe *K*-edge were carried out at a k-range of 2.6-12.5 Å^{-1} and at the Ni *K*-edge 2.6-14.5 Å^{-1}. Errors were estimated from a 68 % confidence interval.

Table S4. Edge positions and oxidation states obtained from edge position and from M-O coordination distances. The parameters were obtained from XAS measurements in the quasi-in situ setup at 20 K.

as-prepared (before OER)				
	K-edge	Edge position /eV	Ox. State from *K*-edge pos.	Ox. State from from d(M-O)
$Ni_{100}(OH)_2$	Ni	8342.8	2.2	2.1
$Ni_{65}+ Fe_{35}$ p.m.	Ni	8342.6	2.1	2.1
$Ni_{65}Fe_{35}$ co-s.	Ni	8342.6	2.1	2.1
$Fe_{100}(OOH)$	Fe	7124.4	3.0	3.5
$Ni_{65}+ Fe_{35}$ p.m.	Fe	7124.6	3.1	3.3
$Ni_{65}Fe_{35}$ co-s.	Fe	7124.7	3.1	3.3
@ catalytic OER potential (1.63 V_{RHE}) in 0.1 M KOH				
	K-edge	Edge position /eV	Ox. State from *K*-edge pos.	Ox. state from d(M-O)
$Ni_{100}(OH)_2$	Ni	8345.9	4.0	3.7
$Ni_{65}+ Fe_{35}$ p.m.	Ni	8342.5	2.1	2.1
$Ni_{65}Fe_{35}$ co-s.	Ni	8342.6	2.1	2.1
$Fe_{100}(OOH)$	Fe	7124.9	3.1	3.4
$Ni_{65}+ Fe_{35}$ p.m.	Fe	7124.3	3.0	3.4
$Ni_{65}Fe_{35}$ co-s.	Fe	7124.7	3.1	3.2

The oxidation states were extracted from reference compounds from Görlin et al. [16] The edge positions in this work were extracted using the step-integral method.[27] Only the first two shells were accounted for in the fits.

References

1. L. Trotochaud, S. L. Young, J. K. Ranney and S. W. Boettcher, Journal of the American Chemical Society, 2014, 136, 6744–6753.
2. M. Barra, M. Haumann, P. Loja, R. Krivanek, A. Grundmeier and H. Dau, Biochemistry, 2006, 45, 14523-14532.
3. M. Risch, F. Ringleb, M. Kohlhoff, P. Bogdanoff, P. Chernev, I. Zaharieva and H. Dau, Energy & Environmental Science, 2015, 8, 661-674.
4. A. Bergmann, E. Martinez-Moreno, D. Teschner, P. Chernev, M. Gliech, J. F. de Araujo, T. Reier, H. Dau and P. Strasser, Nat Commun, 2015, 6, 1-9.
5. A. L. Ankudinov, B. Ravel, J. J. Rehr and S. D. Conradson, Physical Review B, 1998, 58, 7565-7576.
6. J. J. Rehr and R. C. Albers, Reviews of Modern Physics, 2000, 72, 621-654.
7. M. Risch, K. Klingan, J. Heidkamp, D. Ehrenberg, P. Chernev, I. Zaharieva and H. Dau, Chemical Communications, 2011, 47, 11912-11914.
8. H. Yin, L. Jiang, P. Liu, M. Al-Mamun, Y. Wang, Y. L. Zhong, H. Yang, D. Wang, Z. Tang and H. Zhao, Nano Res., 2018, 11, 3959-3971.
9. E. Lee, A.-H. Park, H.-U. Park and Y.-U. Kwon, Ultrasonics Sonochemistry, 2018, 40, 552-557.
10. B. Li, S. Chen, J. Tian, M. Gong, H. Xu and L. Song, Nano Res., 2017, 10, 3629-3637.
11. C. Tang, H.-S. Wang, H.-F. Wang, Q. Zhang, G.-L. Tian, J.-Q. Nie and F. Wei, Advanced Materials, 2015, 27, 4516-4522.
12. R. D. L. Smith, M. S. Prevot, R. D. Fagan, S. Trudel and C. P. Berlinguette, Journal of the American Chemical Society, 2013, 135, 11580-11586.
13. J. Qi, W. Zhang, R. Xiang, K. Liu, H.-Y. Wang, M. Chen, Y. Han and R. Cao, Advanced Science, 2015, 2, 1500199.
14. M. Görlin, M. Gliech, J. Ferreira de Araújo, S. Dresp, A. Bergmann and P. Strasser, Catalysis Today, 2015, 262, 65-73.
15. M. Görlin, J. Ferreira de Araújo, H. Schmies, D. Bernsmeier, S. Dresp, M. Gliech, Z. Jusys, P. Chernev, R. Kraehnert, H. Dau and P. Strasser, Journal of the American Chemical Society, 2017, 139, 2070-2082.
16. M. Görlin, P. Chernev, J. Ferreira de Araújo, T. Reier, S. Dresp, B. Paul, R. Krähnert, H. Dau and P. Strasser, Journal of the American Chemical Society, 2016, 138, 5603-5614.
17. X. Zhu, C. Tang, H.-F. Wang, Q. Zhang, C. Yang and F. Wei, Journal of Materials Chemistry A, 2015, 3, 24540-24546.
18. F. Dionigi, T. Reier, Z. Pawolek, M. Gliech and P. Strasser, ChemSusChem, 2016, 9, 962-972.
19. Z. Lu, W. Xu, W. Zhu, Q. Yang, X. Lei, J. Liu, Y. Li, X. Sun and X. Duan, Chemical Communications, 2014, 50, 6479-6482.
20. M. Gong, Y. Li, H. Wang, Y. Liang, J. Z. Wu, J. Zhou, J. Wang, T. Regier, F. Wei and H. Dai, Journal of the American Chemical Society, 2013, 135, 8452-8455.
21. Y. Xu, Y. Hao, G. Zhang, Z. Lu, S. Han, Y. Li and X. Sun, RSC Advances, 2015, 5, 55131-55135.
22. S. Dresp and P. Strasser, ChemCatChem, 2018, 10, 4162-4171.
23. S. Dresp, F. Luo, R. Schmack, S. Kuhl, M. Gliech and P. Strasser, Energy & Environmental Science, 2016, 9, 2020-2024.
24. M. W. Louie and A. T. Bell, Journal of the American Chemical Society, 2013, 135, 12329-12337.
25. X. Lu and C. Zhao, Nature Communications, 2015, 6, 1-7.
26. F. Dionigi and P. Strasser, Advanced Energy Materials, 2016, 6, 1600621-n/a.
27. H. Dau, P. Liebisch and M. Haumann, Anal Bioanal Chem, 2003, 376, 562-583.